

MOSAIC: Generating Consistent, Privacy-Preserving Scenes from Multiple Depth Views in Multi-Room Environments

Zhixuan Liu¹

Haokun Zhu¹

Rui Chen¹

Jonathan Francis^{1,2}

Soonmin Hwang³

Ji Zhang¹

Jean Oh¹

¹Carnegie Mellon University ²Bosch Center for AI ³Hanyang University

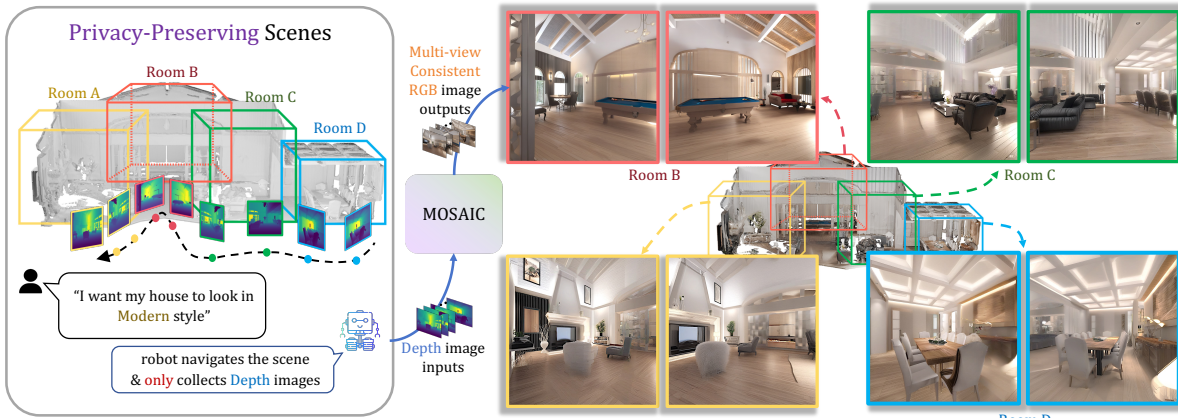


Figure 1. For privacy-preserving scenarios where RGB collection is restricted, MOSAIC generates consistent RGB images from depth data captured along robot paths, guided by text prompts. These outputs further enable 3D reconstruction of multi-room environments.

Abstract

We introduce a novel diffusion-based approach for generating privacy-preserving digital twins of multi-room indoor environments from depth images only. Central to our approach is a novel **Multi-view Overlapped Scene Alignment with Implicit Consistency (MOSAIC)** model that explicitly considers cross-view dependencies within the same scene in the probabilistic sense. MOSAIC operates through a novel inference-time optimization that avoids error accumulation common in sequential or single-room constraint in panorama-based approaches. MOSAIC scales to complex scenes with zero extra training and provably reduces the variance during denoising processes when more overlapping views are added, leading to improved generation quality. Experiments show that MOSAIC outperforms state-of-the-art baselines on image fidelity metrics in reconstructing complex multi-room environments. Project page is available at: <https://mosaic-cmubig.github.io>.

1. Introduction

Autonomous scene reconstruction is a crucial capability in robotics and computer vision [1, 15, 22, 23], with applica-

tions spanning virtual reality, architectural design, and AI-driven simulation. However, existing multi-view 3D reconstruction methods rely heavily on capturing RGB images, which poses significant privacy risks in sensitive environments such as hospitals, factories, elder care facilities, and private residences. Capturing RGB data in these settings can inadvertently expose personal information [29, 44], limiting the practicality of generative AI solutions for real-world deployments where visual privacy must be preserved.

A promising solution for privacy-sensitive environments involves deploying mobile robots that collect only geometric data, such as depth images: this strategy preserves the scene’s structural layout while preventing the capture of sensitive texture information. In order to create digital replicas of these scenes, we need algorithms that are capable of generating high quality, multiview-consistent sequential images that align with ground truth geometry, while maintaining visual coherence across viewpoints.

Various approaches for scene level multiview image generation have been proposed, with autoregressive generation techniques [7, 8, 13, 41, 42] representing the current mainstream trend. These approaches leverage powerful inpainting models to iteratively render unseen parts of the scene from sequential camera perspectives. However, these ap-

proaches exhibit style drift, where images generated for initial viewpoints often differ stylistically from those produced when revisiting the same location from different angles, creating visual inconsistencies. Moreover, warp-and-inpainting methods frequently encounter depth misalignment issues, leading to compounding errors over sequential generations [21, 33]. Unlike prior methods that perform diffusion synchronization tasks [2, 9, 16, 18, 20] in constrained settings (limited viewpoint variations), our task requires coherence between viewpoints based on arbitrary trajectory features, extensive perspective changes, and spatial discontinuities. This fundamental distinction makes existing methods ineffective for complex multi-room environments with widely-varying camera positions.

To address these limitations, we introduce **M**ulti-view **O**verlapped **S**cene **A**lignment with **I**mplicit **C**onsistency (MOSAIC), a novel approach that achieves multi-view consistent RGB image generation from depth data, without compromising privacy in scene level, and while remaining robust to arbitrary egocentric perspective changes across multi-room environments. Rather than requiring extensive training on arbitrary trajectories, MOSAIC operates through a novel multiview inference-time optimization that ensures cross-view consistency during the diffusion process. By minimizing projection differences between overlapping views at each denoising step, our method guarantees visual coherence across the entire scene. A key advantage of MOSAIC is its ability to reduce variance and improve image-depth alignment as more overlapping views are added—the opposite behavior to current autoregressive approaches, which accumulate errors over time. Moreover, we propose a depth-weighted optimization, which naturally prioritizes information from optimal viewpoints, and a pixel-space refinement mechanism which ensures that latent-space consistency translates to visual harmony in the final output. Importantly, MOSAIC scales effortlessly to complex multi-room environments without additional training, making it practical for complex real-world applications. Our experiments demonstrate superior performance over existing methods across multiple metrics, establishing a new state-of-the-art for scene level multi-view image generation with geometric priors.

Our contributions are summarized as follows:

1. We propose MOSAIC, a novel diffusion-based model for multi-view-consistent image generation via explicit modeling of cross-view dependencies.
2. We propose a novel multi-view inference-time optimization as a practical sampling strategy that scales to complex scenes and more depth views with no extra training.
3. We show theoretically that with more overlapping depth views, MOSAIC reduces the variance of generation process, mitigating error accumulations in current autoregressive multi-view image generation pipelines.

4. We introduce depth-weighted projection loss and pixel-space refinement to enforce visual coherence. Extensive experiments demonstrate that MOSAIC generalizes across diverse viewpoints, significantly outperforming state-of-the-art methods in generation quality.

2. Related Work

Diffusion-Guided Scene-Level Multi-view Generation.

Recent advances in 2D diffusion-based generative models [11, 30, 32, 43] have catalyzed significant progress in scene-level multiview image generation—particularly in the use of autoregressive generation techniques that leverage warping and inpainting mechanisms for, e.g., scene completion [7, 8, 13, 41, 42]. These mechanisms can introduce style drift errors where images in later iterations differ stylistically from the initial ones, leading to artifacts and distortions. Alternative approaches attempt to maintain style consistency by generating panoramic representations using off-the-shelf diffusion models [19, 31, 33, 37]. While these methods achieve internal coherence, they cannot handle multiple rooms with complex layouts or flexible camera trajectories, limiting their practicality in the real world. Recent video diffusion models demonstrate promising capabilities for generating temporally consistent image sequences [4, 12, 40, 45]. However, they do not apply to our task due to the inability to incorporate depth conditions and limited tolerance against perspective changes. Our method, on the other hand, explicitly models cross-view consistency and generalizes to arbitrary viewpoints without imposing layout constraints.

Diffusion Synchronization. Several works have explored synchronization techniques for diffusion models [2, 9, 16, 18, 20] to achieve consistency across multiple outputs. However, existing approaches primarily address specialized cases: panoramic view generation [2, 16, 18], orthogonal transformations [9], or object-level consistency with evenly distributed camera positions and well established UV map [16, 20]. Our work addresses a fundamentally different challenge: maintaining consistent image generation across scene-level camera trajectories with arbitrary viewpoints and significant perspective variations. In this complex setting, naive averaging of denoising features fails to preserve cross-view consistency due to the non-orthogonal nature of the transformations and the extensive variance in viewpoint geometry.

Diffusion Inference-Time Optimization. To circumvent the need for large-scale model fine-tuning, several approaches have explored test-time optimization with directional guidance. Diffusion-TTA [26] adapts discriminative models using pre-trained generative diffusion models, updating parameters through gradient backpropagation at inference time. Other methods [24, 25, 35] compute directional controls for single-instance generation (music, im-

ages) by calculating directional losses during diffusion and back-propagating to update denoising features. While these methods focus on intra-level control with easily quantifiable directions, our approach is the first to propose multi-channel test-time optimization for cross-view control using self-provided directional guidance. This novel approach enables us to maintain consistency across arbitrary viewpoints without requiring additional training, addressing the fundamental limitations of existing methods when applied to complex multi-room environments.

3. Problem Definition

We seek to acquire digital replicas of real-world, multi-room indoor environments in a privacy-preserving manner. To safeguard privacy, we refrain from collecting sensitive real RGB data and capture only geometric structures instead. From these structures, we generate *synthetic* RGB data—producing complex, photorealistic scenes that closely align with reality while ensuring no actual environmental details are directly revealed. In this work, we assume that the geometric structures are collected as multiple depth images $\{d^{[1]}, \dots, d^{[N]}\}$ by mobile robots deployed to real-world scenes. To fully cover multi-room environments, the mobile robot plans proper camera pose sequences to ensure overlapping views. Namely, for each $d^{[i]}$, there must exist some area that is also covered by at least one other view $d^{[j]} (j \neq i)$. From $\{d^{[i]}\}_{i \in [N]}$, we are interested in generating corresponding RGB images $\{x^{[i]}\}_{i \in [N]}$ that are multi-view consistent: overlapping depth views must lead to consistent RGB outputs where they overlap in \bar{x} . Namely, for each pixel p in \bar{x} that is covered by multiple depth views, i.e., $I_p := \{i \in [N] \mid p \in d^{[i]}\}$, the RGB output should agree:

$$x^{[i]}[p] = x^{[j]}[p] = \bar{x}[p], \forall i, j \in I_p, i \neq j \quad (1)$$

Then the generated RGB would form a complete 3D multi-room scene \bar{x} once warped by the cameras poses $\{T^{[i]}\}_{i \in [N]}$ (e.g., $\bar{x} = \sum_{i \in [N]} T^{[i]} x^{[i]}$).

4. Method: MOSAIC

4.1. Preliminaries

Denoising Diffusion Implicit Models (DDIM) [32] train a generative model $p_\theta(z_0)$ to approximate a data distribution $q(z_0)$ given samples $z \in \mathcal{Z}$ from q . DDIM considers the following non-Markovian inference model:

$$q_\sigma(z_{1:T} \mid z_0) := q_\sigma(z_T \mid z_0) \prod_{t=2}^T q_\sigma(z_{t-1} \mid z_t, z_0) \quad (2)$$

where $\sigma \in \mathbb{R}_{\geq 0}^T$ is a real vector and $z_{1:T}$ are latent variables in \mathcal{Z} . The inference process $q_\sigma(z_{t-1} \mid z_t, z_0)$ is parameterized by a decreasing sequence $\alpha_{1:T} \in (0, 1]^\top$. To

approximate $q(z_0)$, DDIM learns a generative process

$$p_\theta(z_{0:T}) := p_\theta(z_T) \prod_{t=1}^T p_\theta^{(t)}(z_{t-1} \mid z_t). \quad (3)$$

Starting from a prior $p_\theta(z_T) = \mathcal{N}(0, I)$, z_t is sampled by $p_\theta^{(t)}(z_{t-1} \mid z_t) = q_\sigma(z_{t-1} \mid z_t, f_\theta^{(t)}(z_t))$, where

$$f_\theta^{(t)}(z_t) := \left(z_t - \sqrt{1 - \alpha_t} \cdot \epsilon_\theta^{(t)}(z_t) \right) / \sqrt{\alpha_t} \quad (4)$$

predicts z_0 with a noise prediction model $\epsilon_\theta^{(t)}$. Learning is performed by optimizing the standard variational objective

$$J_\sigma(\epsilon_\theta) := \mathbb{E}_{z_{0:T} \sim q_\sigma} [\log q_\sigma(z_{1:T} \mid z_0) - \log p_\theta(z_{0:T})] \quad (5)$$

In this work, we generate RGB images from depth views d , via ControlNet [43]: $\epsilon_\theta^{(t)}(z_t, d)$. In addition, we sample latent RGB representations z from p_θ which can later be decoded into full images via a pre-trained VAE decoder [17].

In short, the generation process we consider is

$$z_0^{[i]} \sim p_\theta(z_0, d^{[i]}), x^{[i]} = g(z_0^{[i]}) \text{ for } i \in [N]. \quad (6)$$

For clarity, we drop the depth dependency $d^{[i]}$ in notations in the rest of this paper. While the generation of a single image x_i can be readily solved via depth-conditioned diffusion models [43], the generation of complete scenes from multiple depth images remains unsolved.

4.2. MOSAIC Formulation

Intuitively, the sampling procedure in Eq. (6) would generate inconsistent RGB views because the generative process p_θ is trained with independent samples $z_0 \sim q(z_0)$. In our case, however, the samples $z_0^{[1:N]}$ are indeed *dependent* since they are taken from the same complete scene \bar{z}_0 . To fundamentally address the consistency issue, our key insight is to *explicitly model such dependency by incorporating extra projection-based conditionals* $q(z_0^{[i]} \mid \bar{z}_0)$ in the inference procedures. In practice, given \bar{z}_0 , $z_0^{[i]}$ can be collected by simply sampling a camera pose with projection function $\pi^{[i]}$ and setting $z_0^{[i]} = \pi^{[i]}(\bar{z}_0)$; subsequent latents $z_{1:T}^{[i]}$ can be sampled as usual. The updated inference procedure for N depth views from the same scene \bar{z}_0 can be rewritten from Eq. (2) as:

$$q_\sigma(z_{0:T}^{[1:N]} \mid \bar{z}_0) = \prod_{i \in [N]} q(z_0^{[i]} \mid \bar{z}_0) q_\sigma(z_{1:T}^{[i]} \mid z_0^{[i]}). \quad (7)$$

The corresponding generative process can be extended to

$$p_{\theta,\phi}(z_{0:T}^{[1:N]}, \bar{z}_0) = p_\phi(\bar{z}_0 \mid z_0^{[1:N]}) \prod_{i \in [N]} p_\theta(z_{0:T}^{[i]}), \quad (8)$$

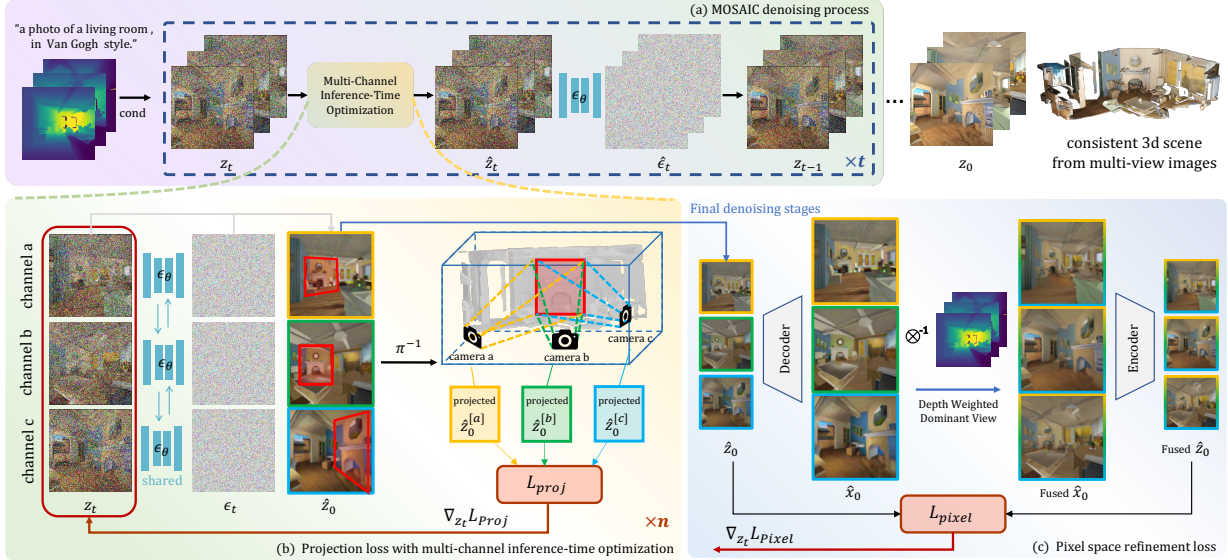


Figure 2. **MOSAIC Overview.** MOSAIC implements a multi-channel denoising framework, as illustrated in (a). We formulate the training objective and address it through projection loss with inference-time optimization (b). In the final denoising phase, a pixel space refinement loss enforces precise RGB consistency constraints (c).

where ϕ parameterizes the reverse process of image projection $q(z_0^{[i]} | \bar{z}_0)$. We name the model $p_{\theta, \phi}$ as **M**ulti-view **O**verlapped **S**cene **A**lignment with **I**mplicit **C**onsistency (MOSAIC), which can be learned by minimizing:

$$J_{\sigma, \text{MOSAIC}}(\epsilon_{\theta}, \phi) := \mathbb{E}_{(z_{0:T}^{[1:N]}, \bar{z}_0) \sim q_{\sigma}} \left[\log q_{\sigma} \left(z_{0:T}^{[1:N]} | \bar{z}_0 \right) - \log p_{\theta, \phi} \left(z_{0:T}^{[1:N]}, \bar{z}_0 \right) \right]. \quad (9)$$

4.3. Sampling from MOSAIC with Multi-Channel Inference-Time Optimization

While MOSAIC captures the dependency between depth views from the same scene, training directly using Eq. (9) is infeasible for two reasons: (a) optimizing the expectation in Eq. (9) via stochastic batches can be computationally intractable, since sufficient combinations of N views are required even from a single scene. Meanwhile, N should be sufficiently large to effectively cover multi-room environments; and (b) $p_{\theta, \phi}$ trained with some fixed N cannot easily generalize to various depth view numbers which further limits the applicability. Hence, we desire a tractable strategy to sample from MOSAIC that is also compatible with an arbitrary number of depth views N . Factorizing q_{σ} using Eq. (7) and $p_{\theta, \phi}$ using Eq. (8), we obtain:

$$\begin{aligned} J_{\sigma, \text{MOSAIC}}(\epsilon_{\theta}, \phi) &\equiv \sum_{i \in [N]} \underbrace{\mathbb{E}_{q_{\sigma}} \left[\log q_{\sigma} \left(z_{1:T}^{[i]} | z_0^{[i]} \right) - \log p_{\theta} \left(z_{0:T}^{[i]} \right) \right]}_{J_{\sigma}^{[i]}(\epsilon_{\theta}) \text{Eq. (5)}} \\ &\quad - \mathbb{E}_{q_{\sigma}} \left[\log p_{\phi}(\bar{z}_0 | z_0^{[1:N]}) \right]. \end{aligned} \quad (10)$$

Note that $p_{\phi}(\bar{z}_0 | z_0^{[1:N]})$ essentially approximates the posterior of the projection operation in forward process and evaluates how well the original scene \bar{z}_0 is reconstructed from separate views with some parameterization ϕ . Hence, we can reasonably set p_{ϕ} to have an inverse exponential dependency on the total re-projection error:

$$p_{\phi}(\bar{z}_0 | z_0^{[1:N]}) \propto \exp(-\sum_i \|\bar{z}_0 - f_{\phi}^{[i]}(z_0^{[i]})\|) \quad (11)$$

where $f_{\phi}^{[i]}$ projects individual views back to the original and error is considered within the back projected region. Hence the second term in Eq. (10) can be written as $\mathbb{E}_{q_{\sigma}} [\sum_{i \in [N]} \|\bar{z}_0 - f_{\phi}^{[i]}(z_0^{[i]})\|]$. Since \bar{z}_0 is in general unavailable, we can instead minimize the total projected cross-view error:

$$J_{\text{Proj}}(\phi) = \mathbb{E}_{q_{\sigma}} [\sum_{i,j} \|f_{\phi}^{[i]}(z_0^{[i]}) - f_{\phi}^{[j]}(z_0^{[j]})\|] \geq 0 \quad (12)$$

Hence, Eq. (10) is equivalent to

$$J_{\sigma, \text{MOSAIC}}(\epsilon_{\theta}, \phi) \equiv \sum_{i \in [N]} J_{\sigma}^{[i]}(\epsilon_{\theta}) + J_{\text{Proj}}(\phi). \quad (13)$$

Although it is impractical to directly train $p_{\theta, \phi}$ using Eq. (13), it is possible to approximate the samples from $p_{\theta, \phi}$ by fine-tuning the output of pre-trained models p_{θ} , e.g., Latent Diffusion Model (LDM) [30]. We observe that for MOSAIC, $p_{\theta, \phi}$ fits trajectories $z_{1:T}^{[1]}, \dots, z_{1:T}^{[N]}$ that are mutually dependent at each step $t = 1, \dots, T$ through $z_0^{[1:N]}$, while such dependency is missing from LDM p_{θ} . Furthermore, this dependency is exactly captured by $J_{\text{Proj}}(\phi)$. If $p_{\theta, \phi}^*$ optimally solves $J_{\sigma, \text{MOSAIC}}$ and $z_0^{[1:N]} \sim p_{\theta, \phi}^*$, there must exist some \bar{z}_0 and corresponding projections $\pi^{[1:N]}$ such that

$z_0^{[i]} = \pi^{[i]}(\bar{z}_0)$, $\forall i \in [N]$. Then, $J_{\text{Proj}}(\phi)$ must have been minimized to 0 with $f_{\phi^*}^{[i]} = (\pi^{[i]})^{-1}$, $\forall i$. In other words, samples from an ideal MOSAIC model should have zero projected cross-view error in expectation as long as $f_{\phi}^{[i]}$ exactly matches the inverse projection $(\pi^{[i]})^{-1}$. While it is generally hard to fit an inverse projection, it is unnecessary in our case because the ground truth projections $\pi^{[1:N]}$ are directly available when collecting depth conditions $d^{[1:N]}$ ¹.

Hence, we can approximately sample from MOSAIC by fine-tuning LDM (i.e., p_{θ}) output at each denoising step $t - 1$ by solving the following *inference-time optimization* through gradient decent:

$$\min_{z_{t-1}^{[1:N]}} L_{\text{Proj}}(z_{t-1}^{[1:N]}) \text{ s.t. } z_{t-1,\text{init}}^{[i]} \sim p_{\theta}^{(t)}(z_{t-1}^{[i]} | z_t^{[i]}), \quad (14)$$

where the empirical projection loss is given by

$$L_{\text{Proj}}(z_t^{[1:N]}) = \sum_{i,j} \|(\pi^{[i]})^{-1}(\hat{z}_0^{[i]}) - (\pi^{[j]})^{-1}(\hat{z}_0^{[j]})\|. \quad (15)$$

$\hat{z}_0^{[i]}$ is the estimated $z_0^{[i]}$ from $z_t^{[i]}$, i.e., $\hat{z}_0^{[i]} = f_{\theta}^{(t)}(z_t^{[i]})$.

Depth Weighted Projection Loss. When calculating L_{Proj} , we observe that depth information provides a natural weighting mechanism for view contributions. For points visible from multiple views, the view with smaller depth value (i.e., closest to the camera) likely provides more accurate RGB information due to higher sampling density and reduced occlusion. To incorporate this insight, we modify our projection loss to weight view contributions based on their relative depth values:

$$L_{\text{Proj}}^{\text{PW}}(z_t^{[1:N]}) = \sum_{i,j} w_{i,j} \cdot \|(\pi^{[i]})^{-1}(\hat{z}_0^{[i]}) - (\pi^{[j]})^{-1}(\hat{z}_0^{[j]})\| \quad (16)$$

where $w_{i,j}$ weights the importance of consistency between views i and j based on their relative depths. To prioritize views with smaller depth values, we employ weighting scheme:

$$w_{i,j} = \frac{\exp(-\alpha \cdot (\pi^{[i]})^{-1} d^{[i]})}{\exp(-\alpha \cdot (\pi^{[i]})^{-1} d^{[i]}) + \exp(-\alpha \cdot (\pi^{[j]})^{-1} d^{[j]})}, \quad (17)$$

where α is a hyperparameter controlling the selectivity of the weighting. With this formulation, when aggregating across all views, the final RGB values for overlapping regions will naturally favor views with minimal depth values.

4.4. Pixel Space Refinement Loss

While our projection loss effectively ensures consistency in latent space, the non-linear nature of the VAE [17] decoder

¹With mobile robots, $\pi^{[i]}$ can be computed from the camera/robot poses in the world coordinate when taking each depth view $d^{[i]}$.

means that consistency in latent space does not necessarily translate to pixel-space consistency. This discrepancy is particularly pronounced when projection transformations are far from orthogonal. We address this issue through a pixel space refinement process during the final denoising stages. For each view i , we decode its predicted latent into pixel space: $\hat{x}^{[i]} = g(\hat{z}_0^{[i]})$. It is infeasible to calculate L_{Proj} in pixel space, because back-propagation through multi-channel VAE decoder poses computation difficulties. We propose to warp these decoded images between views and compute representations for each view point by depth-weighted fusing the overlapped views:

$$w_{ij} = \frac{\exp(-\alpha \cdot \pi_{ij} d^{[j]})}{\sum_{k=1}^N \exp(-\alpha \cdot \pi_{ik} d^{[k]})}, \quad x^{[i]*} = \sum_{j=1}^N w_{ij} \cdot \hat{x}^{[j]} \quad (18)$$

where α control the selectivity of weighting and π_{ij} is the image warping from j view to i view. These optimal pixel-space representation are re-encoded to latent space: $z_0^{[i]*} = \beta \cdot f(x^{[i]*})$. The Pixel Space Refinement Loss is defined as:

$$L_{\text{Pixel}} = \sum_{i=1}^N \|\hat{z}_0^{[i]} - z_0^{[i]*}\| \quad (19)$$

This directly addresses the latent-to-pixel mapping inconsistencies by forcing latent representations to align with those derived from optimally blended pixel-space images. We utilize the L_{Pixel} at the final denoising stages.

4.5. Properties of MOSAIC

Training-free inference time scale-up. The sampling scheme in Eq. (14) essentially consists of two parts: (a) encouraging multi-view consistency via L_{Proj} which is defined for an arbitrary number of views N ; and (b) progressing the reverse process by invoking LDM independently on each view. Hence, unlike full training using Eq. (9), sampling from MOSAIC is agnostic of N , allowing our generation process to easily scale and adapt to larger scenes with more views during inference time, with no extra training.

Variance reduction for pre-trained LDMs. Since LDMs are normally pre-trained in scale, we can roughly view them to have zero prediction error in expectation. However, as will be shown later, LDMs can generate results with varying quality (e.g., in terms of depth preservation) due to the stochasticity of the denoising process, which can cause errors to accumulate until the whole process fails eventually in the warp-inpainting approach. To this regard, one important advantage of MOSAIC is its ability to *stabilize the denoising process given more overlapping views*. This can be seen by analyzing the expected variance of a scene \bar{z}_0 given a varying number of views $z_0^{[1:N]}$ that overlap. Consider a

Table 1. Quantitative evaluation with Kernel Inception Distance (KID), CLIPQA⁺, CLIPScore (CS) and CLIPConsistency(CC).

| Method | KID ↓ | CS ↑ | CIQA ↑ | CC ↑ |
|-------------------|----------------|---------------|---------------|--------------|
| Warp-Inpaint [21] | 0.04646 | 0.6849 | 0.6517 | 29.93 |
| MVDiffusion [34] | 0.03640 | 0.7016 | 0.6025 | 29.41 |
| SceneCraft [39] | 0.07697 | 0.7011 | 0.4531 | 27.68 |
| Text2Room [13] | 0.08594 | 0.6618 | 0.4388 | 27.34 |
| MOSAIC (ours) | 0.03391 | 0.7166 | 0.6526 | 30.85 |

partition $z_0^{[1:N]} = \{z_0^{[I_1]}, z_0^{[I_2]}\}$ where $I_1 \cup I_2 = \{1, \dots, N\}$,

$$\begin{aligned} \Sigma(\bar{z}_0 | z_0^{[I_1]}) &= \mathbb{E}[\Sigma(\bar{z}_0 | z_0^{[I_1]}, z_0^{[I_2]})] + \underbrace{\Sigma(\mathbb{E}[\bar{z}_0 | z_0^{[I_1]}, z_0^{[I_2]}])}_{\Sigma \text{ explained by } z_0^{[I_2]}} \\ &\succeq \mathbb{E}[\Sigma(\bar{z}_0 | z_0^{[I_1]}, z_0^{[I_2]})]. \end{aligned} \quad (20)$$

Taking expectation over $z_0^{[I_1]}$, we have

$$\mathbb{E}[\Sigma(\bar{z}_0 | z_0^{[1:N]})] \preceq \mathbb{E}[\Sigma(\bar{z}_0 | z_0^{[I_1]})]. \quad (21)$$

Namely, when conditioned on more views $z_0^{[I_2]}$, the variance of the final output \bar{z}_0 reduces in expectation by an amount positively related to the overlap between \bar{z}_0 and $z_0^{[I_2]}$ ². The same applies when $z_0^{[1:N]}$ is replaced by estimates from intermediate $z_t^{[1:N]}$, hence the variance reduction happens during the entire denoising process.

5. Experimental Setup

Navigation Agent Autonomous Data Collection. To obtain testing data, we deployed an indoor navigation robot to explore various indoor scenes, collecting depth information via onboard sensors while recording precise camera poses along its trajectory. This approach ensures aligned trajectory-based inputs with baseline methods [13, 21, 34, 39]. To evaluate generalizability, we gathered data across 16 HM3D [28] and 5 MP3D [6] scenes. For trajectory sample details, please refer to Appendix. To generate captions for these depth images, we visualized the collected depth data and utilized a VLM: ChatGPT-4o [5] to provide contextually relevant scene descriptions. This results in 2011 depth data, camera pose, caption pairs in total.

Baselines. We compare our approach against state-of-the-art methods of multiview image generation with geometric priors, including MVDiffusion [34], Warp-Inpaint [21], and SceneCraft [39]. Although SceneCraft shares different condition settings, where its input is the semantic map and the depth map of the bounding box, we create the layout of the bounding box according to our dataset for fair comparison. We evaluate semantic quality against Text2Room [13], a specialized method for indoor scene generation.

²The amount reduced represents the variability of \bar{z}_0 due to changes in $z_0^{[I_2]}$, which is higher when $z_0^{[I_2]}$ covers more area in \bar{z}_0 .

Table 2. Cross-view consistency analysis.

| Method | Warped PSNR ↑ | Warped Ratio ↑ |
|--------------|---------------|----------------|
| GT | 25.45 | 1.00 |
| MVDiffusion | 13.58 | 0.53 |
| Warp-Inpaint | 22.00 | 0.86 |
| Ours Pixel | 25.30 | 0.99 |

Evaluation metrics. The goal of multiview image generation with depth prior is to produce images that maintain consistency in overlapping regions, while preserving image quality, style coherence, and accurate geometric alignment. To evaluate image consistency, we follow MVDiffusion [34] by calculating Warped PSNR [14] and Warped Ratio. We assess image quality using Kernel Inception Distance (KID) [3] and CLIPQA⁺ [36], and measure image-text alignment with CLIPScore [10] and CLIPConsistency [27].

6. Results

6.1. Evaluation Against Baselines

Qualitative Comparisons. As shown in Fig. 3, MOSAIC produces more coherent and photorealistic results than existing approaches using identical depth inputs. MVDiffusion [34] lacks cross-view consistency and cannot generalize to stylistic prompts like “in Van Gogh style.” The warp-and-inpainting approach [21] generates acceptable initial frames but suffers from progressive style drift and accumulating errors during sequential generation. SceneCraft [39] fails to capture complex environment layouts and produces blurry artifacts due to its NeRF-based methodology. Text2Room [13], built on the warp-and-inpainting pipeline, exhibits noticeable patchwork-like seams from inpainting inconsistencies as well as the depth misalignment. In contrast, MOSAIC maintains consistency across viewpoints while preserving fidelity to both depth information and style prompts, effectively eliminating boundary artifacts through our depth-weighted projection mechanism.

Quantitative Comparisons. Tab. 1 presents a quantitative comparison of our proposed method against several state-of-the-art approaches, including Warp-and-Inpainting [21], MVDiffusion [34], SceneCraft [39], and Text2Room [13], on the multi-view consistent image generation task. Our method achieves the lowest KID score (↓) of 0.0391 and highest CS (↑) of 0.7166, CIQA of 0.6526, and CC of 30.85, outperforming other methods by a significant margin in all image quality metrics. In addition to the quality improvement, Tab. 2 demonstrates our exceptional cross-view consistency with a Warped PSNR of 25.30 and Warped Ratio of 0.99, approaching ground truth performance (25.45, 1.00) and substantially outperforming competing methods. Although MVDiffusion achieves a competitive KID score of

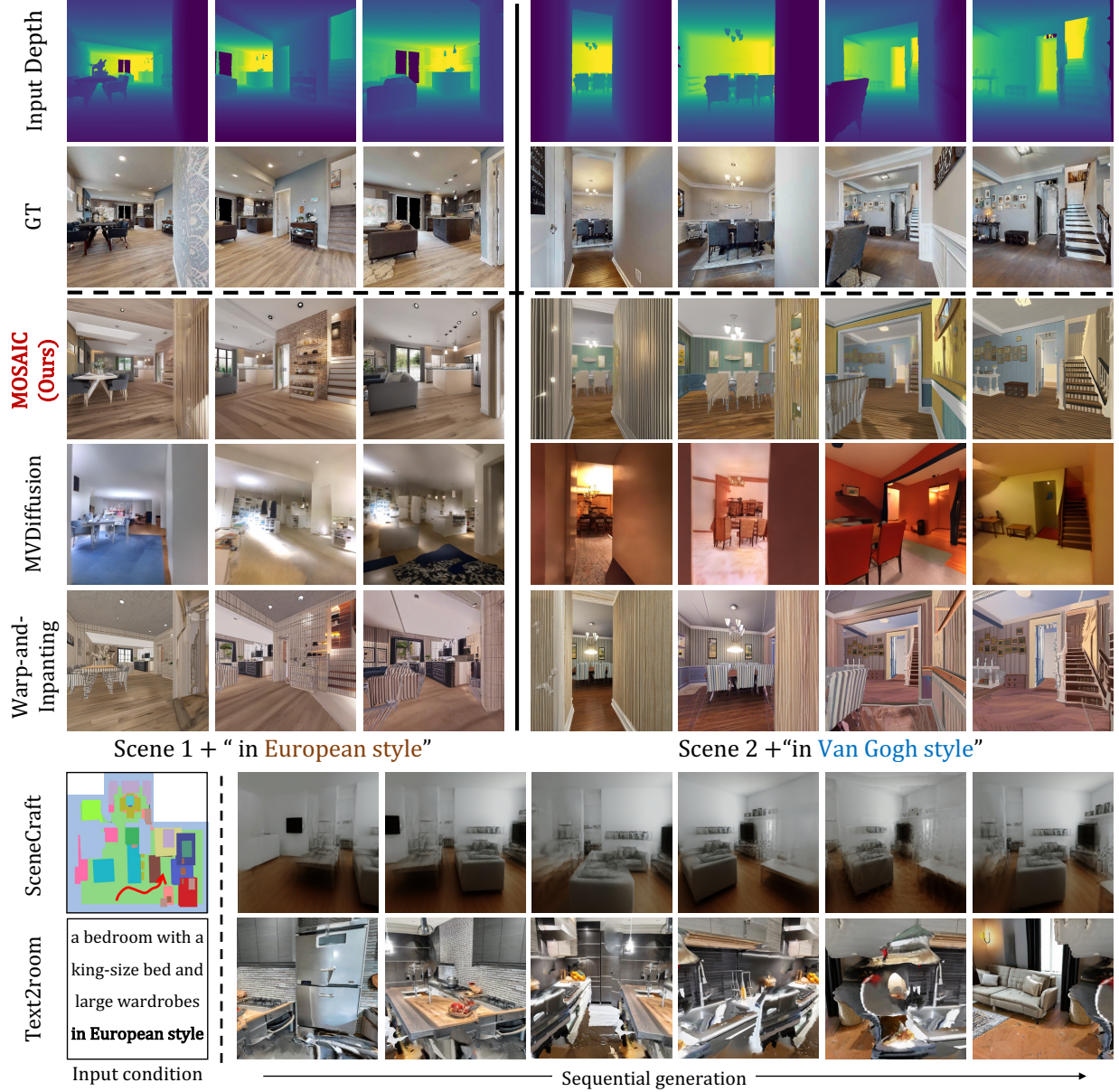


Figure 3. Qualitative comparison with multi-view generation baselines. More results are available in the supplementary material.

0.0640, its cross-view consistency is highly limited with a Warped PSNR of only 13.58. Our approach achieves outstanding performance in both image quality and cross-view consistency compared with state-of-the-art methods.

6.2. Ablation Study

Effect of MOSAIC Objective and Multi-Channel Test-Time Optimization.

We formulate a naive ablation baseline by extending [16] to scene-level multi-view image generation, averaging each denoising latent prediction z_0 without our multi-channel inference time optimization for MOSAIC objectives. As shown in Tab. 3, this naive approach yields poor results with the highest KID score and lowest

consistency metrics. Fig. 4 reveals significant issues—the second row exhibits severe blurry artifacts (red boxes) and compromised cross-view consistency. In contrast, our full model with pixel space refinement delivers exceptional performance, achieving the lowest KID score, highest consistency metrics, and superior cross-view alignment (green boxes). These results demonstrate that MOSAIC objective optimization is crucial for multi-room environments with significant viewpoint variations, where naive averaging fails to maintain both visual quality and geometric coherence.

Effect of Pixel Space Refinement. Tab. 3 shows how pixel space refinement enhances MOSAIC’s performance. This refinement yields notable improvements in both perceptual

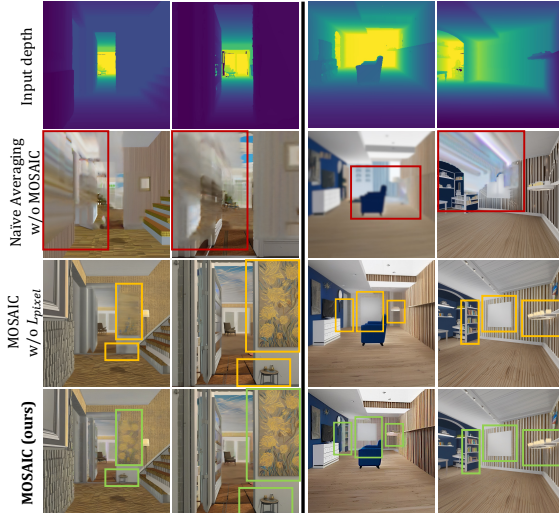


Figure 4. Qualitative ablation results. **Red:** artifacts; **orange:** pixel space texture misaligned; **Green:** with pixel space loss, full model (MOSAIC) aligns the pixel space color.

Table 3. Ablation: Image Quality and Consistency

| | Image Quality | | | | Image Consistency | |
|----------------------------|----------------|---------------|---------------|--------------|-------------------|---------------|
| | KID ↓ | CS ↑ | CIQA ↑ | CC ↑ | PSNR ↑ | Ratio ↑ |
| w/o test-time optimization | 0.06715 | 0.7285 | 0.5725 | 31.08 | 15.74 | 0.6185 |
| w/o key frame selection | 0.03920 | 0.6746 | 0.6733 | 29.25 | 24.67 | 0.9692 |
| w/o L_{Pixel} | 0.04273 | 0.7249 | 0.6797 | 31.26 | 23.02 | 0.9045 |
| MOSAIC (ours full) | 0.03391 | 0.7166 | 0.6526 | 30.85 | 25.30 | 0.9940 |

quality (lower KID) and cross-view consistency (approaching ground truth metrics). Fig. 4 illustrates this improvement between 3rd and 4th row: texture misalignments (yellow) become properly aligned (green) after refinement.

Effect of Trajectory Key Frame Selection. We evaluate our region-coverage sampling strategy against uniform trajectory sampling in Tab. 3. While image quality and consistency metrics remain comparable between approaches, text-image alignment noticeably decreases with uniform sampling. This occurs because uniform sampling frequently captures frames facing flat walls, challenging VLMs to generate precise captions. Furthermore, pretrained ControlNet models tend to hallucinate textures with such depth inputs, creating semantic misalignments. Our strategic key-frame selection effectively balances information-rich viewpoints with sufficient overlap, yielding more accurate text-conditioned generation without sacrificing consistency.

Multi-Views for better RGB-Depth Alignment. Traditional scene-level generation approaches employ warp-and-inpainting strategies that suffer from error accumulation—initial RGB-depth misalignments compound through sequential generation. In contrast, our theoretical analysis in Eq.21 establishes that leveraging multi-view depth conditioning inherently reduces variance, yielding representations that more faithfully reflect ground truth geometry. Tab. 4 empirically validates this theoretical insight: as viewpoint count increases, normalized MSE between ground truth depth and generated image depth (estimated via Depth



Figure 5. Second column: Single-view generation creates artifacts (in red) contradicting ground truth depth. Third column: MOSAIC achieves superior depth alignment (in green).

Table 4. Assessing the effect of number of depth views, NMSE stands for normalized MSE.

| | NMSE ↓ | CS ↑ | KID ↓ |
|-------------|-----------------|---------------|----------------|
| single view | 0.018630 | 0.6874 | 0.06123 |
| two views | 0.013453 | 0.6883 | 0.06022 |
| three views | 0.011961 | 0.6986 | 0.06709 |
| four views | 0.011269 | 0.7100 | 0.07833 |

Anything [38]) demonstrates consistent decline. Fig. 5 visually confirms this phenomenon—single-view conditioning (middle column) produces hallucinated elements that misalign with ground truth geometry (red boxes), while MOSAIC’s two-view approach (right column) maintains precise geometric fidelity. Our analysis further reveals an inflection point in the quality-viewpoint curve, with text-image alignment steadily improving across viewpoints while perceptual quality peaks at 2-3 highly overlapping views. This finding suggests an optimal operating point that balances computational efficiency with generation quality.

7. Conclusion

We proposed MOSAIC, the first training-free multi-view consistent image generation pipeline that operates at scene level. MOSAIC handles arbitrary numbers of views along any trajectory, adapting to extensive camera viewpoint changes. It employs a depth-weighted projection loss and a pixel-space refinement process to maintain visual coherence across complex multi-room environments, making it well-suited for privacy-sensitive applications. We developed a novel multi-channel inference-time optimization procedure that minimizes cross-view projection errors, which we mathematically prove to be equivalent to the ideal learning objective. We showed theoretically and demonstrated experimentally that by intelligently fusing multi-view information, MOSAIC substantially improves alignment between generated RGB images and ground truth depth and significantly outperforms state-of-the-art methods—addressing the error accumulation issues of current autoregressive multi-view image generation pipelines.

Acknowledgements

This work was supported in part by NSF IIS-2112633.

References

- [1] Sunday Amatare, Gaurav Singh, Raul Shakya, Aavash Kharel, Ahmed Alkhateeb, and Debashri Roy. Dt-radar: Digital twin assisted robot navigation using differential ray-tracing, 2024. 1
- [2] Omer Bar-Tal, Lior Yariv, Yaron Lipman, and Tali Dekel. Multidiffusion: Fusing diffusion paths for controlled image generation, 2023. 2
- [3] Mikołaj Bińkowski, Danica J Sutherland, Michael Arbel, and Arthur Gretton. Demystifying mmd gans. *arXiv preprint arXiv:1801.01401*, 2018. 6
- [4] Andreas Blattmann, Tim Dockhorn, Sumith Kulal, Daniel Mendelevitch, Maciej Kilian, Dominik Lorenz, Yam Levi, Zion English, Vikram Voleti, Adam Letts, et al. Stable video diffusion: Scaling latent video diffusion models to large datasets. *arXiv preprint arXiv:2311.15127*, 2023. 2
- [5] Tom B. Brown, Benjamin Mann, Nick Ryder, Melanie Subbiah, Jared Kaplan, Prafulla Dhariwal, Arvind Neelakantan, Pranav Shyam, Girish Sastry, Amanda Askell, Sandhini Agarwal, Ariel Herbert-Voss, Gretchen Krueger, Tom Henighan, Rewon Child, Aditya Ramesh, Daniel M. Ziegler, Jeffrey Wu, Clemens Winter, Christopher Hesse, Mark Chen, Eric Sigler, Mateusz Litwin, Scott Gray, Benjamin Chess, Jack Clark, Christopher Berner, Sam McCandlish, Alec Radford, Ilya Sutskever, and Dario Amodei. Language models are few-shot learners, 2020. 6
- [6] Angel Chang, Angela Dai, Thomas Funkhouser, Maciej Halber, Matthias Nießner, Manolis Savva, Shuran Song, Andy Zeng, and Yinda Zhang. Matterport3d: Learning from rgbd data in indoor environments, 2017. 6
- [7] Jaeyoung Chung, Suyoung Lee, Hyeongjin Nam, Jaerin Lee, and Kyoung Mu Lee. Luciddreamer: Domain-free generation of 3d gaussian splatting scenes. *arXiv preprint arXiv:2311.13384*, 2023. 1, 2
- [8] Rafail Fridman, Amit Abecasis, Yoni Kasten, and Tali Dekel. Scenescape: Text-driven consistent scene generation. *Advances in Neural Information Processing Systems*, 36:39897–39914, 2023. 1, 2
- [9] Daniel Geng, Inbum Park, and Andrew Owens. Visual anagrams: Generating multi-view optical illusions with diffusion models, 2024. 2
- [10] Jack Hessel, Ari Holtzman, Maxwell Forbes, Ronan Le Bras, and Yejin Choi. CLIPScore: a reference-free evaluation metric for image captioning. In *EMNLP*, 2021. 6
- [11] Jonathan Ho, Ajay Jain, and Pieter Abbeel. Denoising diffusion probabilistic models. *Advances in neural information processing systems*, 33:6840–6851, 2020. 2
- [12] Jonathan Ho, Tim Salimans, Alexey Gritsenko, William Chan, Mohammad Norouzi, and David J Fleet. Video diffusion models. *Advances in Neural Information Processing Systems*, 35:8633–8646, 2022. 2
- [13] Lukas Höller, Ang Cao, Andrew Owens, Justin Johnson, and Matthias Nießner. Text2room: Extracting textured 3d meshes from 2d text-to-image models. In *Proceedings of the IEEE/CVF International Conference on Computer Vision*, pages 7909–7920, 2023. 1, 2, 6
- [14] Alain Horé and Djemel Ziou. Image quality metrics: Psnr vs. ssim. In *2010 20th International Conference on Pattern Recognition*, pages 2366–2369, 2010. 6
- [15] Bernhard Kerbl, Georgios Kopanas, Thomas Leimkühler, and George Drettakis. 3d gaussian splatting for real-time radiance field rendering, 2023. 1
- [16] Jaihoon Kim, Juil Koo, Kyeongmin Yeo, and Minhyuk Sung. Syncnweedies: A general generative framework based on synchronized diffusions, 2024. 2, 7
- [17] Diederik P Kingma and Max Welling. Auto-encoding variational bayes, 2022. 3, 5
- [18] Yuseung Lee, Kunho Kim, Hyunjin Kim, and Minhyuk Sung. Syncdiffusion: Coherent montage via synchronized joint diffusions, 2023. 2
- [19] Wenrui Li, Fucheng Cai, Yapeng Mi, Zhe Yang, Wangmeng Zuo, Xingtao Wang, and Xiaopeng Fan. Scenedreamer360: Text-driven 3d-consistent scene generation with panoramic gaussian splatting, 2024. 2
- [20] Yuxin Liu, Minshan Xie, Hanyuan Liu, and Tien-Tsin Wong. Text-guided texturing by synchronized multi-view diffusion, 2023. 2
- [21] Mikonvergence. Controlnetinpaint, 2023. Accessed: March 2025. 2, 6
- [22] Ben Mildenhall, Pratul P. Srinivasan, Matthew Tancik, Jonathan T. Barron, Ravi Ramamoorthi, and Ren Ng. Nerf: Representing scenes as neural radiance fields for view synthesis, 2020. 1
- [23] Zak Murez, Tarrence Van As, James Bartolozzi, Ayan Sinha, Vijay Badrinarayanan, and Andrew Rabinovich. Atlas: End-to-end 3d scene reconstruction from posed images. In *European conference on computer vision*, pages 414–431. Springer, 2020. 1
- [24] Zachary Novack, Julian McAuley, Taylor Berg-Kirkpatrick, and Nicholas J. Bryan. Ditto: Diffusion inference-time t-optimization for music generation, 2024. 2
- [25] Quynh Phung, Songwei Ge, and Jia-Bin Huang. Grounded text-to-image synthesis with attention refocusing, 2023. 2
- [26] Mihir Prabhudesai, Tsung-Wei Ke, Alexander C. Li, Deepak Pathak, and Katerina Fragkiadaki. Diffusion-tta: Test-time adaptation of discriminative models via generative feedback, 2023. 2
- [27] Alec Radford, Jong Wook Kim, Chris Hallacy, Aditya Ramesh, Gabriel Goh, Sandhini Agarwal, Girish Sastry, Amanda Askell, Pamela Mishkin, Jack Clark, et al. Learning transferable visual models from natural language supervision. In *International conference on machine learning*, pages 8748–8763. PMLR, 2021. 6
- [28] Santhosh K. Ramakrishnan, Aaron Gokaslan, Erik Wijmans, Oleksandr Maksymets, Alex Clegg, John Turner, Eric Undersander, Wojciech Galuba, Andrew Westbury, Angel X. Chang, Manolis Savva, Yili Zhao, and Dhruv Batra. Habitat-matterport 3d dataset (hm3d): 1000 large-scale 3d environments for embodied ai, 2021. 6

- [29] Siddharth Ravi, Pau Climent-Pérez, and Francisco Florez-Revuelta. A review on visual privacy preservation techniques for active and assisted living, 2021. [1](#)
- [30] Robin Rombach, Andreas Blattmann, Dominik Lorenz, Patrick Esser, and Björn Ommer. High-resolution image synthesis with latent diffusion models. In *Proceedings of the IEEE/CVF conference on computer vision and pattern recognition*, pages 10684–10695, 2022. [2, 4](#)
- [31] Jonas Schult, Sam Tsai, Lukas Höllein, Bichen Wu, Jialiang Wang, Chih-Yao Ma, Kunpeng Li, Xiaofang Wang, Felix Wimbauer, Zijian He, Peizhao Zhang, Bastian Leibe, Peter Vajda, and Ji Hou. Controlroom3d: Room generation using semantic proxy rooms, 2023. [2](#)
- [32] Jiaming Song, Chenlin Meng, and Stefano Ermon. Denoising diffusion implicit models. In *International Conference on Learning Representations*, 2021. [2, 3](#)
- [33] Liangchen Song, Liangliang Cao, Hongyu Xu, Kai Kang, Feng Tang, Junsong Yuan, and Yang Zhao. Roomdreamer: Text-driven 3d indoor scene synthesis with coherent geometry and texture, 2023. [2](#)
- [34] Shitao Tang, Fuyang Zhang, Jiacheng Chen, Peng Wang, and Yasutaka Furukawa. MVDiffusion: Enabling holistic multi-view image generation with correspondence-aware diffusion. In *Thirty-seventh Conference on Neural Information Processing Systems*, 2023. [6](#)
- [35] Yun-Yun Tsai, Fu-Chen Chen, Albert Y. C. Chen, Junfeng Yang, Che-Chun Su, Min Sun, and Cheng-Hao Kuo. GDA: Generalized diffusion for robust test-time adaptation, 2024. [2](#)
- [36] Jianyi Wang, Kelvin CK Chan, and Chen Change Loy. Exploring clip for assessing the look and feel of images. In *Proceedings of the AAAI conference on artificial intelligence*, pages 2555–2563, 2023. [6](#)
- [37] Qi Wang, Ruijie Lu, Xudong Xu, Jingbo Wang, Michael Yu Wang, Bo Dai, Gang Zeng, and Dan Xu. Roomtex: Texturing compositional indoor scenes via iterative inpainting, 2024. [2](#)
- [38] Lihe Yang, Bingyi Kang, Zilong Huang, Xiaogang Xu, Jiashi Feng, and Hengshuang Zhao. Depth anything: Unleashing the power of large-scale unlabeled data, 2024. [8](#)
- [39] Xiuyu Yang, Yunze Man, Junkun Chen, and Yu-Xiong Wang. Scenecraft: Layout-guided 3d scene generation. *Advances in Neural Information Processing Systems*, 37: 82060–82084, 2025. [6](#)
- [40] Zhuoyi Yang, Jiayan Teng, Wendi Zheng, Ming Ding, Shiyu Huang, Jiazheng Xu, Yuanming Yang, Wenqi Hong, Xiaohan Zhang, Guanyu Feng, Da Yin, Xiaotao Gu, Yuxuan Zhang, Weihan Wang, Yean Cheng, Ting Liu, Bin Xu, Yuxiao Dong, and Jie Tang. Cogvideox: Text-to-video diffusion models with an expert transformer, 2024. [2](#)
- [41] Hong-Xing Yu, Haoyi Duan, Charles Herrmann, William T. Freeman, and Jiajun Wu. Wonderworld: Interactive 3d scene generation from a single image, 2024. [1, 2](#)
- [42] Hong-Xing Yu, Haoyi Duan, Junhwa Hur, Kyle Sargent, Michael Rubinstein, William T. Freeman, Forrester Cole, Deqing Sun, Noah Snavely, Jiajun Wu, and Charles Herrmann. Wonderjourney: Going from anywhere to everywhere, 2024. [1, 2](#)
- [43] Lvmin Zhang, Anyi Rao, and Maneesh Agrawala. Adding conditional control to text-to-image diffusion models. In *Proceedings of the IEEE/CVF international conference on computer vision*, pages 3836–3847, 2023. [2, 3](#)
- [44] Yiqin Zhao, Sheng Wei, and Tian Guo. Privacy-preserving reflection rendering for augmented reality, 2022. [1](#)
- [45] Zangwei Zheng, Xiangyu Peng, Tianji Yang, Chenhui Shen, Shenggui Li, Hongxin Liu, Yukun Zhou, Tianyi Li, and Yang You. Open-sora: Democratizing efficient video production for all. *arXiv preprint arXiv:2412.20404*, 2024. [2](#)